

Tunable Thin Elasto-Drops

A. Eddi,¹ S. Perrard,¹ and J. Zhang^{1,*}

¹*PMMH, CNRS, ESPCI Paris, Université PSL, Sorbonne Université, Université de Paris, F-75005, Paris, France*

(Dated: December 4, 2025)

We present an experimental method to fabricate centimetric thin elastic capsules with highly uniform thickness and negligible bending stiffness using silicone elastomers. In our experiments, the capsules thickness is tunable at fabrication, while internal pressure and hoop (circumferential) stress are adjustable via hydrostatic inflation once the capsules are filled and immersed in water. Capsules mechanics are probed through hydro-elastic waves generated by weak mechanical perturbations at the capsule interface. By analyzing the surface wave dynamics in the Fourier domain, we extract the in-plane stress and demonstrate that the hydro-elastic waves are exclusively governed by hoop stress. This establishes a direct analogy with liquid drops characterised by an effective surface tension, allowing the capsules to be modeled as large-scale “elasto-drops” with an inflation and thickness tunable effective surface tension. Our work demonstrates that elasto-drops serve as a robust model system for parametric studies of large-scale liquid drops with experimentally adjustable surface tension.

INTRODUCTION

Soft particles such as droplets and bubbles deform when subjected to an external flow or during impacts. The deformation in turn governs their dynamics, including impact spreading [1], vortex shedding [2], as well as oscillatory rise dynamics under double confinement [3]. These behaviours are typically quantified using dimensionless numbers such as the Weber number for droplet impacts or drop in flows, which compares inertia and surface tension, the Bond number for buoyancy-driven bubble deformation, which compares gravitational forces and surface tension, or the Cauchy number for soft particles, which compares inertia and elastic modulus. For droplets and bubbles, the accessible ranges of Weber or Bond number are intrinsically limited by surface tension γ , whose values are set by intermolecular forces. While surface tension can span more than an order of magnitude across liquid families (e.g. 10–487 mN/m for common liquids at 20°C) [4], altering γ inevitably modifies other fluid properties such as density and viscosity. As a result, the capillary length remains millimetric for nearly all standard liquids. In addition, the presence of surfactants either naturally or introduced voluntarily can significantly alter the surface tension of fluid pairs [5], which further reduces the effective controllability of the interfacial properties.

Recent experimental advances in the fabrication of hollow elastic shells using elastomers such as VPS (vinyl polysiloxane) or PDMS (polydimethylsiloxane) has allowed a transition from fluid-fluid interface dominated objects such as drops and bubbles to solid and deformable interfaces governed by shell elasticity. Indeed, it is possible to produce elastic spheres with controlled thickness and mechanical properties [6]. Such elasto-capsules have since been employed as model systems in various contexts, including droplet impact dynamics on solid walls [7], or the shear-induced deformation and breakup

of microcapsules [8, 9]. Typically, the recent work by Jambon-Puillet et al. [7] has shown that elastic water capsules can extend the regime of droplet spreading at impact over a Weber number 10 times higher than those with weakly viscous droplets [10], opening a promising route to probe new dynamical regimes for large scale soft particle deformations. However, the elastic capsules studied so far, although highly deformable, are not sufficiently thin for bending stiffness to be entirely negligible, limiting access to the idealized thin-shell, tension-only regime where a strict analogy with liquid droplet capillarity can be drawn.

In this work, we introduce a new method to fabricate thin elastic capsules with controlled size and tunable effective tension. Our approach builds on work showing that elastic membranes strongly modify surface-wave dynamics, as demonstrated in previous studies of hydro-elastic waves on floating elastic sheets, ranging from ice-sheet analogues [11, 12] and elastic wave turbulence [13, 14], to optics and solid-state physics analogues [15–17]. For an elastic plane sheet of thickness h , Young’s modulus E , and Poisson ratio ν , the hydro-elastic wave dynamics in the small-amplitude limit are obtained by coupling the linearized Föppl-von Kármán equations describing the in-plane tension and bending response of the sheet with the Bernoulli equation for an inviscid, irrotational fluid. In the deep-water limit, this coupling yields the standard hydro-elastic dispersion relation $\omega(k)$ [12]

$$\omega^2 = gk + \frac{T}{\rho}k^3 + \frac{D}{\rho}k^5, \text{ with } D = \frac{Eh^3}{12(1-\nu^2)}, \quad (1)$$

where g is the gravity, T the in-plane tension and D the bending modulus. The first term on the right-hand side arises from gravity, while the second and third terms reflect the contributions from in-plane tension and bending rigidity, respectively. For a closed elastic capsule filled with water and fully immersed in water (i.e., a neutrally buoyant capsule), the gravitational term vanishes, and

the relevant in-plane tension reduces to the hoop stress of the spherical membrane. By measuring the dispersion relation of the waves propagating along the capsule surface through simple mechanical vibrations, we directly extract this hoop stress and thus obtain the capsule's effective tension in a simple, non-intrusive way. This provides a robust method to characterize the mechanical response of deformable capsules.

MATERIALS & METHODS

Elasto-drops fabrication

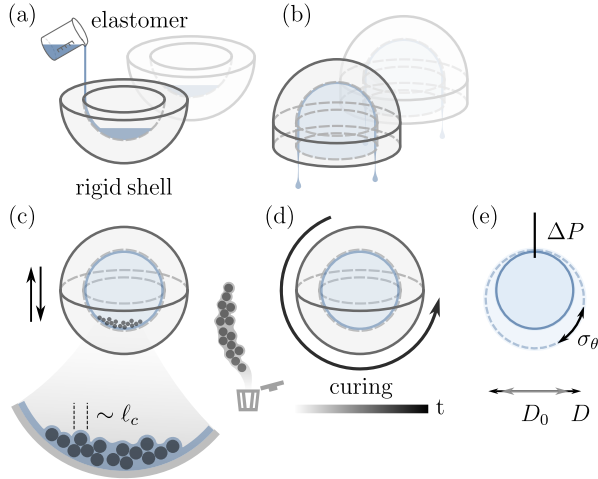


FIG. 1. Fabrication process of the elasto-drop. a–e: Sequence of coating, draining, ball-assisted thinning, curing, demolding and liquid filling.

The elastic shell of uniform thickness was fabricated using a viscous coating technique adapted from established methods [6, 7]. The fabrication process of the elasto-drop is illustrated in Figure 1. We first prepare a polymer solution by mixing equal parts by weight of the silicone base and the catalyst. The resulting mixture has a well-defined pot life during which it remains liquid and workable, allowing it to be poured and shaped in a mold. This is followed by a curing stage, where polymer cross-linking gradually transforms the liquid into a soft elastomer. The pot life of most commercial silicone elastomers ranges from 16 mins to more than 1 hour at 25°C [18]. For applications such as coating in rotation, a longer pot life allows more time to homogenize the thickness of the molded or coated layer, improving shell uniformity. In our case, we use a spherical two-part mold: a polymer solution is first deposited into each plastic hemisphere and spread uniformly across the inner surface. The hemispheres are then placed bottom-down on supporting rings of matching diameter, allowing excess liquid to drain without accumulating along the edge.

To further thin the coating, millimetric plastic balls are introduced, the hemispheres are closed, and the assembly is vigorously shaken so that the balls roll inside and remove additional liquid. After the balls being removed, the hemispheres are sealed and mounted on a planetary rotating platform to cure the elastomer; during this stage, capillary forces smooth out the ball imprints. Once the shell has solidified, it is demolded, and the internal air cavity is replaced by water through a needle puncture. The puncture site is finally sealed with a drop of fast-curing elastomer.

We fabricate the elastic shell using a commercial PDMS-based soft silicone elastomer (Ecoflex 00-30). This elastomer serie has a pot life of 45 mins and a cure time of 1 hour, allowing an thin and uniform distribution of the shell coating, and a weak Young's modulus $E = 62.5 \pm 37.5$ kPa, making the final elasto-drop extremely deformable. The Young's modulus was experimentally deduced from independent tensile testing on a strip sample.

Experimental setup

We have fabricated elasto-drops of an initial external diameter of $D_0 = 42$ mm and three different thicknesses $h_0 = 59.2 \mu\text{m}$, $125.5 \mu\text{m}$ and $185.5 \mu\text{m}$. Thickness values are first estimated from the total capsule mass, measured via precise weighting, and independently validated using white-light colorimetric interferometry. The elasto-drop, filled up with water, is placed at the center of a water tank of dimension $250 \times 250 \times 200$ mm³, as is shown in Figure 2(a). A needle of 1 mm in diameter and 117 mm in length is used to hold the elasto-drop in place. The top of the shell is pierced by the lower tip of a needle and sealed with elastomer, allowing for rapid variation of the liquid volume inside the elasto-drop by injecting or extracting water with a syringe. We are thus able to control the hydrostatic pressure ΔP inside the shell. This pressure due to the inflation can be further associated to the hoop stress σ_θ by $\Delta P = 2h/R\sigma_\theta$ where θ refers to the zenith angle [19].

For spherical elasto-drop inflation, the shell undergoes an a uniform and isotropic deformation (equibiaxial), the tangential strain in the circumferential direction can be simply associated by the radius variation with respect to the initial radius $\varepsilon = (R - R_0)/R$. In our experimental investigations, the elasto-drops were inflated at ten discrete strain increments, spanning a tangential strain from 0 to approximately $\varepsilon \approx 30\%$. Under this weak deformation regime, we expect that the stress remains linearly proportional to the strain $\sigma_\theta = E/(1 - \nu)\varepsilon$ [20].

The needle is firmly mounted to an electromagnetic shaker (LDS V200) that allows to generate mechanical perturbations with controlled frequencies and amplitudes (Fig. 2a). Via the needle, the perturbations are directly

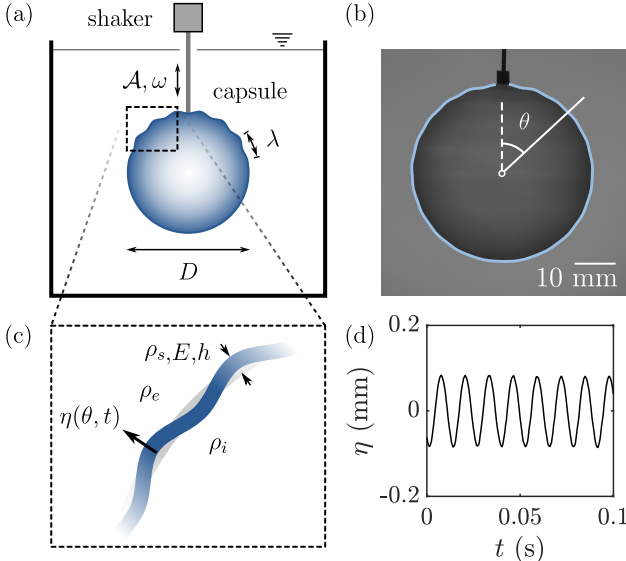


FIG. 2. a: Schematics of the hydro-elastic wave propagation on the surface of a pre-stretched elasto-drop. b: Example of the elasto-drop's surface edge detection, for an elasto-drop of initial thickness $h_0 = 125.5 \mu\text{m}$, inflated at a strain $(R - R_0)/R_0 = 4\%$, under a periodic forcing frequency $f_s = 77.7 \text{ Hz}$. The blue solid line represents the elasto-drop's detected edge. The zenith angle θ varying from 0 to 2π in the clockwise direction is defined with the vertical dashed line passing through the center and a solid line. c: Physical properties of the elastic shell and the surrounding fluids. The surface elevation is in the radial direction of the initially unperturbed sphere. d: Time variation of the surface elevation $\eta(\theta = 0.82, t)$, obtained based on a classical edge detection by image intensity gradient. e: Zenithal variation of the shell's thickness.

transmitted to the top of the elasto-drop's surface and elastic waves propagate along the elasto-drop's surface. The wave propagation being axisymmetric about the vertical axis, the elastic wave can be directly associated to the surface elevation $\eta(\theta, t)$, where θ is the zenith angle (Fig. 2b). To capture the elasto-drop's edge displacement, LED-backlight images of the elasto-drop contour have been recorded using a high-speed camera (Phantom v1840) equipped with a Samyang f2.8/100 optical lens leading to a pixel size of $59 \mu\text{m}$ (Fig. 2b).

To cross validate our elasto-drop's mechanical property extraction from wave measurements, two types of stroking signals were used and are subsequently referred as the *harmonic* and *impulse* forcing. The *harmonic* forcing mode has an analytical expression $A(t) = A_0 \cos(2\pi f_s t)$. For each given strain of elasto-drop, 20 points were recorded with the forcing frequency f_s logarithmically spaced between 10 Hz and 345 Hz. For the *impulse* mode, the capillary tip moves downward from the initial position at rest before reaching a maximum amplitude, then lifts back upward to the starting position. The total time duration of the stroke is around 10

ms.

The recording sampling rate for the *harmonic* mode was varied for each wave stroke frequency to ensure a minimum of 16 images per wave time period $1/f_s$, for a recording duration of at least 100 wave periods. For the *impulse* mode, each recording lasts 2 seconds with a sampling frequency $f_s = 3000 \text{ Hz}$.

We extract and analyse the elasto-drop's spatiotemporal edge elevation in polar coordinates $\eta(\theta, t)$, consistent with wave propagation on a spherical surface. To do so, we used a matlab built-in function *improfile* to sample the image intensity values along a line segment passing through the center of the shell, starting from the vertical top origin where $\theta = 0$ and sweeping clockwise to $\theta = 2\pi$, with a step of $\delta\theta = 0.5^\circ$. At a given angle, the associated elevation is obtained with a classical 1D edge detection method, based on spatial gradient of the intensity variation with a subpixel resolution. A snapshot image of the elasto-drop under *harmonic* forcing at $f_s = 77.7 \text{ Hz}$ is shown in Figure 2(b), the elasto-drop has a strain $(R - R_0)/R_0 = 4\%$. The blue curve corresponds to the extracted edge deformation $\eta(\theta, t)$. The wavy deformation can be seen to be symmetrical about the vertical axis. Due to the attachment mount of the elasto-drop to the capillary tip, the total angular range of the elastic shell is slightly restricted by 4.1° from each end. Figure 2(d) illustrates a time evolution of the local edge displacement in periodic motion at the zenith angle $\theta = 47^\circ$.

RESULTS & DISCUSSION

Fig. 3(a,b) shows snapshots of the typical elasto-drop's surface elevation under two forcing modes, measured at an inflation strain $\varepsilon = 4\%$. The corresponding spatiotemporal amplitudes $\eta(\theta, t)$ are illustrated in Fig. 3(c,d), where the dashed lines indicate the time position of the above shown instantaneous forms. We see on the diagrams that under both forcing modes, waves are emitted from the top ($\theta = 0, 2\pi$), propagate from both ends towards the bottom of the shell, forming a symmetry about the vertical axis ($\theta = \pi$). It is noticeable that for waves under *impulse* forcing (b,d), a single impulsive impact on the elasto-drop generates a large-band of dispersive waves in a broad band of wavelengths.

We now focus on the dispersion relation analyses of the wave dynamics. To this end, we first perform a co-ordinate transformation from the zenith angle θ to the arc length $x = R\theta$, which describes wave propagation in the in-plane (tangential) direction, where R is the unperturbed radius of the elasto-drop. From the spatiotemporal signal $\eta(x, t)$, we compute its Fourier transform $\hat{\eta}(\omega, k)$ in frequency and wavenumber space. For *harmonic* forcing, we identify the dominant wavenumber k_m corresponding to the maximum spectral ampli-

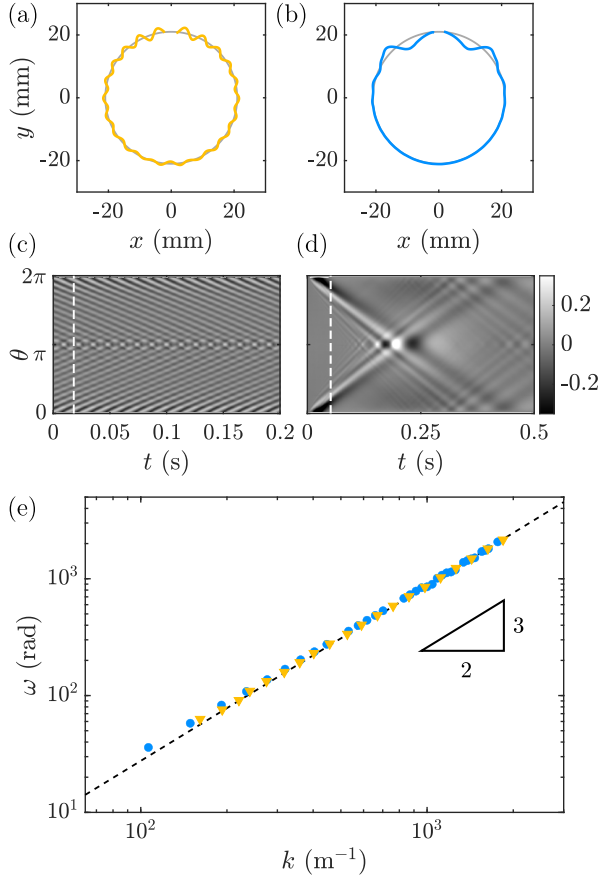


FIG. 3. a,b: Instantaneous shapes of the elasto-drop surface under a-harmonic and b-impulse forcing, radially amplified by a factor of ten for better visibility. c,d: Spatiotemporal diagram of the surface amplitude η as a function of the zenith angle θ . The harmonic forcing frequency reads $f_s = 77.7$ Hz. e: Dispersion relation $\omega(k)$ extracted from the frequency-wavenumber domain of the surface amplitude $\hat{\theta}(\omega, k)$ for harmonic (yellow) and impulse (blue). The dashed lines indicate the power-law fit $\omega = [Tk^3/(2\rho)]^{1/2}$.

tude at each stroke frequency f_s . The extracted pairs (f_s, k_m) are then displayed in Fig. 3(e) as yellow triangles in log-log scale. The same procedure can be applied to waves under impulse forcing; however, in this case multiple frequencies and wavenumbers can be simultaneously excited, since the wave field is inherently multi-spectral. The extracted pairs are illustrated with blue dots. When comparing the extracted dispersion relations from the two forcing modes, we find an excellent agreement. In addition, we plot the theoretical power law $\omega \propto k^{3/2}$, which spans more than a decade in both frequency and wavenumber, consistent with the expected behaviour of tension-dominated waves. We then fit the data with a power law (dashed line) to extract the corresponding tension T .

In our case, in absence of the free surface, the elasto-drop encapsulating water is fully submerged in a water

tank, the gravity term $\omega^2 \sim gk$ vanishes. Moreover, the consistency of our data with the power law $k^{3/2}$ suggests also that the flexural term vanishes. The dispersion relation of the waves then becomes $\omega^2 = T/(\rho_i + \rho_e)k^3$, where both external and internal fluids are water in this case, $\rho = \rho_e = \rho_i$.

Fig. 4(a) shows the extracted tension T as a function of the principle in-plane strain of the inflated elasto-drop, for three different initial shell thicknesses (blue: $h_0 = 59.2 \mu\text{m}$, violet: $125.5 \mu\text{m}$ and orange: $185.5 \mu\text{m}$). We see that increasing either the inflation or the initial thickness of the elasto-drop lead to an increase of its tension.

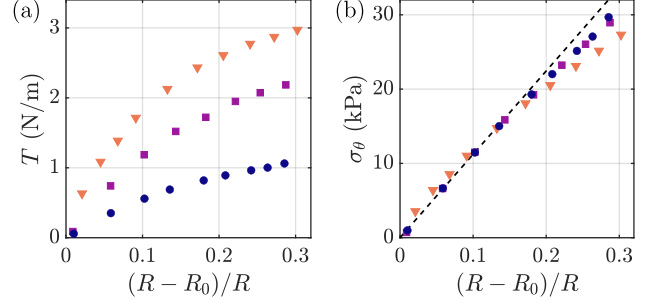


FIG. 4. a: Extracted tension of the elasto-drops, for increasing inflation, as a function of the in-plane strain. blue: $h_0 = 59.2 \mu\text{m}$, violet: $125.5 \mu\text{m}$ and orange: $185.5 \mu\text{m}$. b: Tangential stress σ_θ as a function of the strain.

We now divide the extracted tension by the corresponding shell thickness h at each strain to obtain the in-plane stress σ_θ , as shown in Fig. 4(b). We find that all data collapse on a master line following $\sigma_\theta = E_T/(1-\nu)\varepsilon$, where $E_T = 56 \text{ kPa}$ is the extracted Young's modulus. This value is in good agreement with different works using the same commercial polymer [18, 21–25].

As for the flexural wave, a typical transition wavenumber $k_{TD} = \sqrt{T/D}$ between the flexion and tension waves can be obtained by balancing both terms $(T/2\rho)k^3 = (D/2\rho)k^5$. With a typical extracted values in tension $T = 1 \text{ N/m}$, we find a cutoff wavenumber and frequency $k_{TD} \approx 4.0 \times 10^3 \text{ m}^{-1}$, $f_{TD} \approx 1.3 \times 10^3 \text{ Hz}$ for the thickest tested elasto-drop ($h_0 = 185.5 \mu\text{m}$) and $k_{TD} \approx 2.2 \times 10^4 \text{ m}^{-1}$, $f_{TD} \approx 1.7 \times 10^4 \text{ Hz}$ for the thinnest one ($h_0 = 59.2 \mu\text{m}$). These high values of the cutoff wavenumber and the associated frequency guarantee that the elasto-drops dynamics are soundly dominated by tension waves in the typical frequency range of interest of most potential applications such as interaction with water waves or turbulence. For homogeneous isotropic turbulent (HIT) water flows, a recent review comparing the flow characteristics of major HIT facilities reports that the Kolmogorov length scale η typically falls within 18–620 μm [26]. This yields a corresponding eddy turnover frequency $f_\eta \equiv 1/t_c \sim \varepsilon^{1/3}\eta^{-2/3}$ that lies between 4–446 Hz, where ε refers to the turbulent kinetic energy dissipation rate. Over this frequency range, capsule deforma-

tions in our experiments is entirely governed by surface traction, with other mechanical modes being negligible.

The analogy with liquid drops meet several limitations due to the fundamental substantial difference between a liquid-liquid interface and a solid membrane. For an elasto-drop, the effective surface tension depends on the strain itself, and is therefore not conserved during deformation. This can lead to significant difference between a drop and an elasto-drop dynamics as soon as the deformation exceeds the linear order. Moreover, at large deformations, shape instability may occur, such as the emergence of wrinkles in the presence of local membrane compression [27–29].

CONCLUSIONS

In this paper we present a robust and cost-efficient method for centimetric elasto-drop fabrication with a minimum thickness ratio $h_0/R_0 \approx 2.8 \times 10^{-4}$. To characterize these capsules, we exploit the propagation of surface waves along their membrane under varying inflation rates. At first order, the dispersion of these waves provides direct access to membrane tension, owing to the equivalence between surface tension and elastic tension in the limit of thin membranes undergoing small, linear deformations, allowing to establish an analogy with capillary waves with an efficiently tunable capillary. These highly deformable objects offer a controlled way to decouple size, deformability, fluid density and viscosity, and open the door to the future design of fully tunable viscoelastic particles.

ACKNOWLEDGEMENTS

This work was supported by the Agence Nationale de la Recherche with grants ANR Lascaturb (Grant No. ANR-23-CE30-0043) and ANR TransWaves (Grant No. ANR-24-CE51-3840).

* jishen.zhang@espci.fr

- [1] C. Clanet, C. Béguin, D. Richard and D. Quéré, *Journal of Fluid Mechanics*, 2004, **517**, 199–208.
- [2] G. Mougin and J. Magnaudet, *Physical review letters*, 2001, **88**, 014502.
- [3] L. Pavlov, M. D’angelo, M. Cachile, V. Roig and P. Ern, *Anales AFA*, 2022, pp. 66–70.
- [4] A. W. Adamson, A. P. Gast et al., *Physical chemistry of surfaces*, Interscience publishers New York, 1967, vol. 150.
- [5] J. Eastoe and J. Dalton, *Advances in colloid and interface science*, 2000, **85**, 103–144.
- [6] A. Lee, P.-T. Brun, J. Marthelot, G. Balestra, F. Gallaire and P. M. Reis, *Nature communications*, 2016, **7**, 11155.
- [7] E. Jambon-Puillet, T. J. Jones and P.-T. Brun, *Nature Physics*, 2020, **16**, 585–589.
- [8] E. Häner, M. Heil and A. Juel, *Journal of Fluid Mechanics*, 2020, **885**, A4.
- [9] S. Joung, M. Song and D. Kim, *Physics of Fluids*, 2020, **32**, 113603.
- [10] L. Liu, G. Cai, B. Jiang, B. He and P. A. Tsai, *International Journal of Multiphase Flow*, 2025, 105345.
- [11] B. Auvity, L. Duchemin, A. Eddi and S. Perrard, *arXiv preprint arXiv:2501.04824*, 2025.
- [12] R. M. S. M. Schulkjes, R. Hosking and A. Sneyd, *Journal of Fluid Mechanics*, 1987, **180**, 297–318.
- [13] M. Vernet and E. Falcon, *Physical Review Letters*, 2025, **135**, 024004.
- [14] L. Deike, J.-C. Bacri and E. Falcon, *Journal of Fluid Mechanics*, 2013, **733**, 394–413.
- [15] L. Domino, M. Fermigier, E. Fort and A. Eddi, *Europhysics Letters*, 2018, **121**, 14001.
- [16] L. Domino, M. Fermigier and A. Eddi, *Applied Physics Letters*, 2020, **117**, 063701.
- [17] G. L. Doudic, M. Jafari, J. Barckicke, S. Perrard and A. Eddi, *arXiv preprint arXiv:2407.16454*, 2024.
- [18] J. Vaicekauskaitė, P. Mazurek, S. Vudayagiri and A. L. Skov, *Journal of Materials Chemistry C*, 2020, **8**, 1273–1279.
- [19] C. Ross, J. Bird and A. Little, *Mechanics of solids*, Routledge, 2021.
- [20] L. D. Landau, L. Pitaevskii, A. M. Kosevich and E. M. Lifshitz, *Theory of elasticity: volume 7*, Elsevier, 2012, vol. 7.
- [21] M. Lanoy, F. Lemoult, A. Eddi and C. Prada, *Proceedings of the National Academy of Sciences*, 2020, **117**, 30186–30190.
- [22] A. Delory, F. Lemoult, M. Lanoy, A. Eddi and C. Prada, *The Journal of the Acoustical Society of America*, 2022, **151**, 3343–3358.
- [23] A. Delory, F. Lemoult, A. Eddi and C. Prada, *Extreme Mechanics Letters*, 2023, **61**, 102018.
- [24] A. Delory, D. A. Kiefer, M. Lanoy, A. Eddi, C. Prada and F. Lemoult, *Soft Matter*, 2024, **20**, 1983–1995.
- [25] R. Janardhana, F. Akram, Z. Guler, A. Adaval and N. Jackson, *Materials*, 2025, **18**, 3037.
- [26] L. Beckedorff, G. C. Caridi and A. Soldati, *Review of Scientific Instruments*, 2025, **96**, 025107.
- [27] E. Yariv, P. D. Howell and H. A. Stone, *Journal of Fluid Mechanics*, 2025, **1012**, A12.
- [28] D. Barthès-Biesel, *Comptes Rendus Physique*, 2009, **10**, 764–774.
- [29] V. Kantsler, E. Segre and V. Steinberg, *Physical review letters*, 2007, **99**, 178102.